npj | 2D Materials and Applications

www.nature.com/npj2dmaterials

ARTICLE OPEN

Check for updates

2D transistors rapidly printed from the crystalline oxide skin of molten indium

Andrew B. Hamlin[1], Youxiong Ye[1], Julia E. Huddy[1], Md Saifur Rahman[1] and William J. Scheideler[1]✉

Ultrathin single-nm channels of transparent metal oxides offer unparalleled opportunities for boosting the performance of low power, multifunctional thin-film electronics. Here we report a scalable and low-temperature liquid metal printing (LMP) process for unlocking the ultrahigh mobility of 2-dimensional (2D) InO_x. These continuous nanosheets are rapidly (60 cm s^{-1}) printed over large areas (30 cm^2) directly from the native oxide skin spontaneously formed on molten indium. These nanocrystalline LMP InO_x films exhibit unique 2D grain morphologies leading to exceptional conductivity *as deposited*. Quantum confinement and low-temperature oxidative postannealing control the band structure and electronic density of states of the 2D InO_x channels, yielding thin-film transistors with ultrahigh mobility ($\mu_0 = 67$ cm^2 $V^{-1}s^{-1}$), excellent current saturation, and low hysteresis at temperatures down to 165 °C. This work establishes LMP 2D InO_x as an ideal low-temperature transistor technology for high-performance, large area electronics such as flexible displays, active interposers, and thin-film sensors.

npj 2D Materials and Applications (2022)6:16 ; https://doi.org/10.1038/s41699-022-00294-9

INTRODUCTION

Transparent conducting oxides' exceptional optoelectronic properties have traditionally made them critical electrode materials for state-of-the-art displays, photovoltaics, and smart windows. However, oxides such as InO_x[1], SnO_x[2], InGaZnO[3] (IGZO), and ZnO[4] are also extremely promising as low-temperature processed high mobility semiconductors for driving new thin-film electronics. Emerging applications of conducting oxides to low power switching[5], neuromorphic computing[6], and biosensing[7] can be unlocked by utilizing ultrathin, nm-scale two-dimensional (2D) layers with favorable electrostatics. Among these 2D oxides, ultrathin InO_x displays a unique tendency towards strong surface electron accumulation[8], offering surprisingly high mobility transport in films just one unit cell thick (~1 nm)[9] with outstanding short channel performance for GHz-range circuits[7]. Beyond switching, this high conductivity in combination with high visible range transmittance makes 2D InO_x well suited, for example, as charge selective contacts for an emerging class of heterostructure photodetectors based on MXenes[10], graphdiyne[11] and transition metal dichalcogenides (TMDs)[12]. The functional versatility and low-temperature processing capability of 2D oxides are particularly interesting for heterogeneous 3D integration with low power CMOS circuits[13].

2D conducting oxides could offer their greatest technological advantages for large area flexible electronics due to their high bending strain tolerance[14], but there remains a technological need for scalable deposition of these ultrathin films. Precision vacuum-based methods such as ALD can control nm-scale thickness, but are capital intensive, relatively low-throughput, and challenging to scale to large areas for flexible devices[15]. Large area printing technologies, on the other hand, could enable low-cost flexible device fabrication, but it has proved challenging to achieve both high uniformity and high mobility for ultrathin films[16]. Additionally, although sol-gels and nanoparticles have been developed for printing metal oxides[17,18], there remains a barrier to processing high-performance oxides (>10 cm^2 $V^{-1}s^{-1}$) within the thermal limits of polymer substrates, such as PET and PEN (~200 °C)[19] as precursor decomposition is incomplete below 225 °C[17]. New frontiers in high-performance flexible electronics require advanced low-temperature fabrication strategies to take advantage of the potential of 2D oxides in low-cost, wearable devices.

Liquid metal printing of a new class of van der Waals 2D oxides could overcome these challenges to accelerate high-performance flexible electronics. Liquid metal printing is a vacuum-free route to depositing ultrathin (<5 nm) metal oxide semiconductors generated by spontaneous surface oxidation[20]. This method has been utilized for synthesis of various metal oxides[21] (SnO_2, SbO_x, $InSnO_x$, GaO_x, etc.) for applications to transparent conductive films[14], photodetectors[22,23], as well as switching devices[24]. A powerful feature of liquid metal synthesis distinguishing it from contact-based adhesive 2D material transfer is the liquid metal's *mechanical compliance* which leads to its ability to transfer continuous nanosheets at the cm^2 scale[25]. However, despite the promise of this method, further advances are needed to allow careful tuning of the electronic properties of 2D oxides for new applications by replacing manual 'touch' printing methods[14] and utilizing lower temperatures broadly compatible with polymer substrates.

In this work, we address these challenges by developing 2D InO_x transistors with exceptional switching performance fabricated via a rapid pneumatic liquid metal printing process at unprecedented low temperatures (165 °C). We find that liquid metal printing is a perfect match for an intrinsically conductive oxide, such as InO_x that requires forming ultrathin films to deliver electrostatic control[9]. These devices illustrate the advantages of liquid metal printing (LMP) for forming crystalline and highly conducting films *as deposited*, avoiding insulating intermediate phases and eliminating the thermodynamic barriers posed by precursor decomposition. Leveraging this process, we reveal how these distinctive nanocrystalline morphologies of 2D InO_x lead to its outstanding electronic transport characteristics and through detailed characterization of the electronic density of states we

[1]Thayer School of Engineering, Dartmouth College, Hanover, NH 03755, United States. ✉email: william.j.scheideler@dartmouth.edu

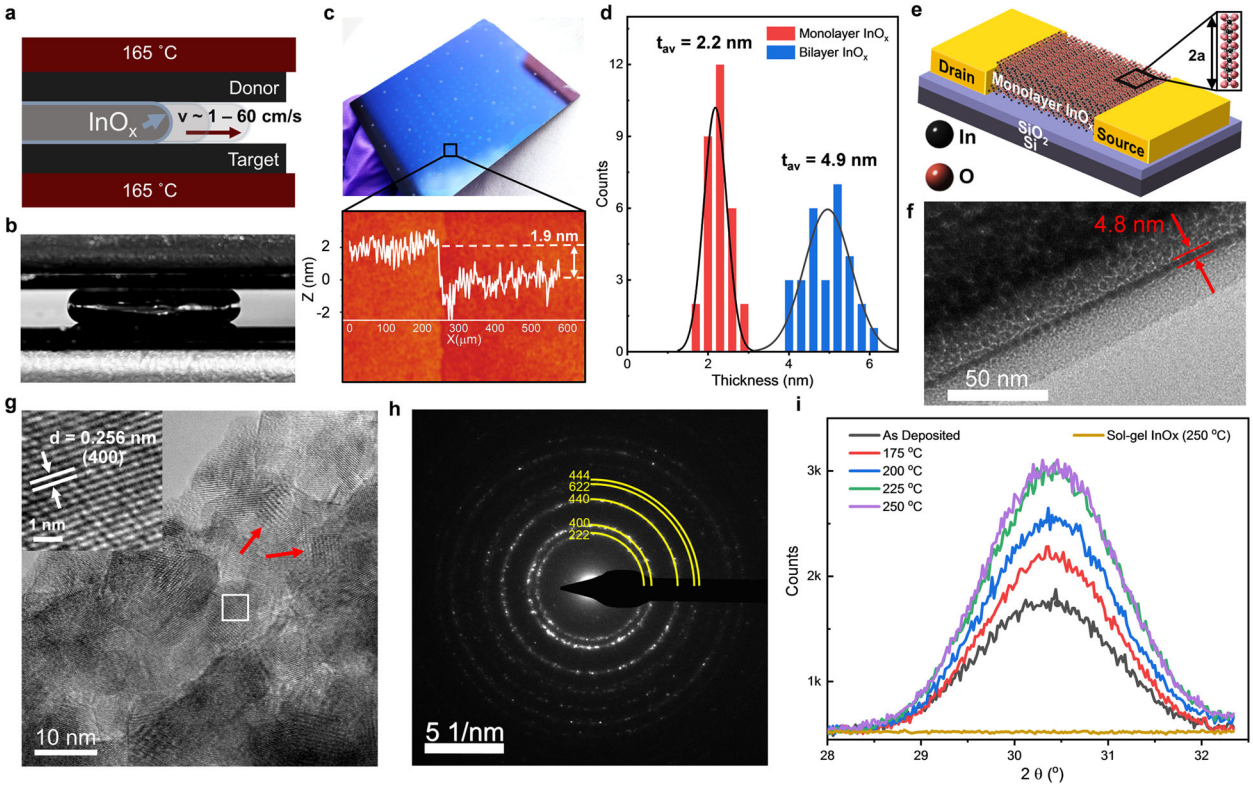

Fig. 1 Liquid metal printing schematic, TEM, and X-ray diffraction studies. a Schematic for liquid metal 2D oxide deposition and **b** photograph of liquid metal droplet during pneumatic pressing process. **c** Large area (30 cm^2) array of 2D InO_x semiconductors (top) with height map (bottom) showing line scan for a monolayer film. **d** Histogram of measured thicknesses for monolayer and bilayer InO_x films. **e** Atomic-scale illustration of monolayer InO_x channel transistor two unit cells thick. **f** Cross-sectional TEM image of 2D InO_x film. **g** HRTEM image of the 250 °C annealed InO_x nanosheet. The inset shows a magnified view of the lattice pattern within a nanograin. Red arrows highlight Moiré fringes. **h** SAED pattern for postannealed bilayer InOx nanosheet. **i** XRD scans of the (222) peak for bilayer InO_x films postannealed at various temperatures.

precisely engineer the electronic structure for high-performance thin-film transistors.

RESULTS & DISCUSSION

Liquid metal printed 2D InO_x

Our liquid metal printing process delivers lower process temperatures (165 °C) than previous work[22] by leveraging a temperature-controlled dual-sided thermomechanical transfer of liquid metal-derived oxide nanosheets. This process (Fig. 1a) relies on the spontaneous growth and subsequent *high-speed* transfer of a nanoscale solid oxide skin on a spreading droplet of liquid indium metal. We apply this process to generate large continuous sheets of InO_x at the 20 cm^2 scale, which are rapidly deposited via the spreading of the liquid metal meniscus (Fig. 1b) at a speed of 1–60 cm s^{-1}, as estimated by slow-motion photography. Our approach of controlling the donor and target substrate temperatures allows for uniform deposition of arrays over large areas (Fig. 1c), as well as process control to modulate the electronic properties of the transferred 2D InO_x films. The printing process can be tuned to produce 2.2 ± 0.3 nm monolayer or 4.9 ± 0.6 nm bilayer nanosheets (Fig. 1d) by utilizing variable donor surfaces, with plastic donors transferring bilayers and smoother SiO_2 donor surfaces transferring monolayer films. Figure 1e illustrates a nanoscale view of thin-film transistors incorporating these 2D semiconducting channels composed of just two unit cells of InO_x. Cross-section of the bilayer specimen was also observed via transmission electron microscopy (TEM), which reveals a thickness of approximately 4.8 nm for the bilayer InO_x films produced with the liquid metal printing method (Fig. 1f).

These ultrathin InO_x films exhibit both highly crystalline and amorphous regions for both monolayer and bilayer depositions. A top-down view of the nanosheets was characterized using high-resolution TEM (HRTEM) to provide further insight into the morphology and crystalline structure of the bilayer InO_x films produced via the liquid metal printing process with and without postannealing (Supplementary Fig. 1). After annealing at 250 °C for 1 h, these films exhibit domains in varying orientations with lateral dimensions of up to 20 nm (Fig. 1g). The Moiré fringes in these TEM images also demonstrate that the overlay of two nanosheets can be clearly deduced for both unannealed and postannealed specimens. TEM-based grain size analysis of the postannealed films (Supplementary Fig. 2), for example, shows a range from 5 to 15 nm, with an average of 8.1 ± 2.6 nm. These grains can be considerably larger in their lateral dimension than the transferred film thickness, a property typically associated with highly ordered materials produced by methods such as pulsed laser deposition (PLD)[26]. The enlarged view in the inset displays well-defined lattice fringes, corresponding to the (400) lattice plane of cubic In_2O_3. The nanocrystalline feature of the nanosheet can also be confirmed by the selected area electron diffraction (SAED) pattern, which exhibits diffraction rings typical of cubic In_2O_3 (Fig. 1h).

X-ray diffraction (XRD) spectra of these films are dominated by a single (222) peak of cubic InO_x for both the monolayer and bilayer films (Supplementary Fig. 3). The average crystallite size predicted by Scherrer analysis of the (222) peak of monolayer films is similar to that of bilayer films, yielding 6.6 nm and 5.9 nm, respectively, with no significant change in crystallite size upon postannealing. This lack of recrystallization of nanosheets separated by a van der Waals gap matches recent reports of liquid metal printed 2D

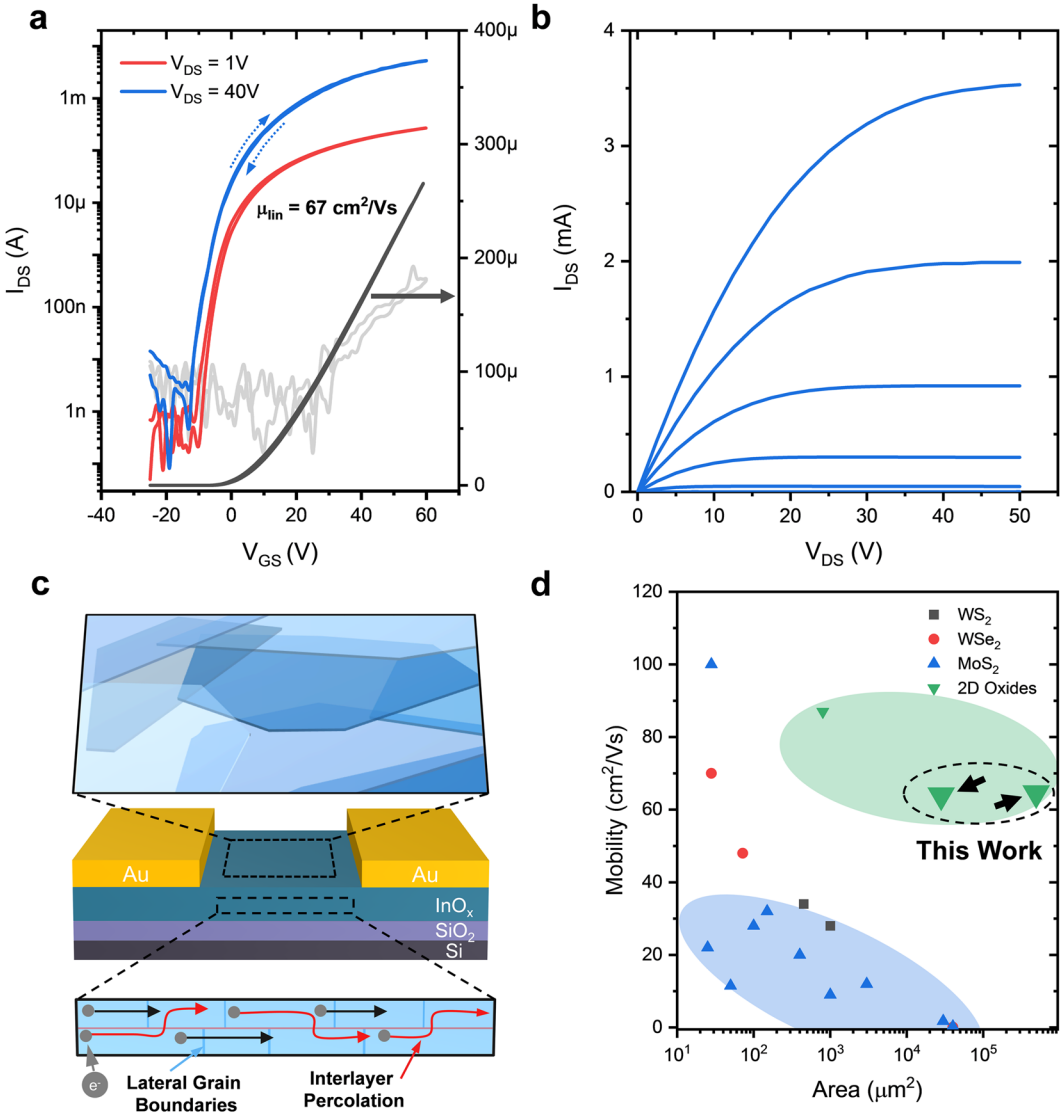

Fig. 2 2D InO_x transistor characteristics and 2D material benchmarking. a Linear and saturation transfer curves for champion bilayer 2D InO_x printed transistor postannealed at 250 °C. **b** Output curves for champion device with Vgs = −10 V to 40 V in 10 V steps. **c** Schematic of device architecture with overlapped 2D bilayer grain structure leading to efficient interlayer electronic transport and high electron mobility. **d**. Mobility comparison between 2D channel materials as a function of device area reported in literature.

indium tin oxide (ITO)[14]. With subsequent annealing, the InO_x (222) peak increases in intensity (Fig. 1i), reaching its highest integrated intensity after approximately 225 °C (Supplementary Fig. 4). For comparison, a control sample of sol-gel synthesized InO_x produced by spin coating was measured by XRD, showing only the amorphous phase even with thermal annealing up to 275 °C (Supplementary Fig. 5). The cubic phase observed in these studies also stands in contrast to recent reports of rhombohedral In_2O_3 formed by liquid metal printing at higher temperatures and in inert environments[25].

These results indicate that a principle advantage of liquid metal printed 2D oxides relative to predominate sol-gel formulations is the ability to achieve crystalline films *as deposited* and avoid hydroxide formation, a known acceptor type defect limiting the conductivity of InO_x[27]. The lack of carbonaceous solvents or metal salt precursors in our liquid metal printing method eliminates the requisite formation of intermediate phases dominated by metal hydroxide bonding. This can be seen in the XPS O1s peaks for spin-coated sol-gel films (Supplementary Fig. 6) which consist of 79% M-OH bonding compared with liquid metal printed films, which show minimal hydroxide content (18% M-OH) (Supplementary Table 1). Our liquid metal printing method provides a method to deposit these ultrathin 2D oxide semiconductors while controlling their electronic properties to achieve high mobility.

2D InO_x thin-film transistors

The liquid metal synthesized 2D InO_x films were integrated into thin-film transistors with exceptional switching performance exceeding those of competing low-temperature solution-processed metal oxide semiconductors. Figure 2a shows the transfer characteristics of the champion InO_x transistor, which exhibits extremely high electron mobility, as well as minimal hysteresis for forward and reverse sweeps after 250 °C post-annealing in air. The linear regime transfer curve exhibits a peak linear mobility reaching a stable value of approximately 67.1 $cm^2 V^{-1}s^{-1}$ (Supplementary Fig. 7) with a threshold voltage (V_t) of approximately 10 V. This remarkable on-state performance is complemented by ideal current saturation as shown in the output curve in Fig. 2b, indicating the absence of back-channel conduction or instability in these high mobility materials.

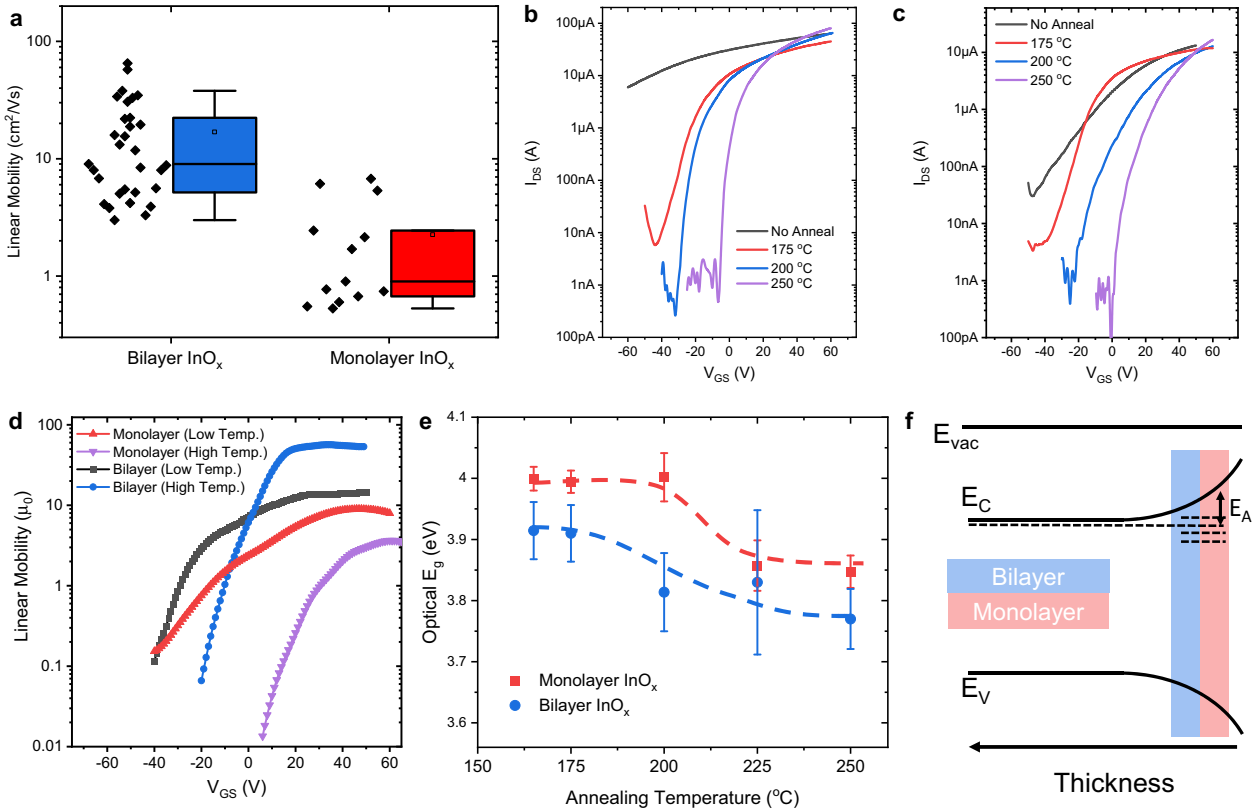

Fig. 3 Transistor performance characteristics and optical properties vs. thermal postannealing. a Linear mobility comparison between bilayer and monolayer InO_x transistors. Representative transfer curves for bilayer (**b**) and monolayer (**c**) printed InO_x transistors on SiO_2 dielectrics, postannealed in air at temperatures from 150 °C to 250 °C. **d** Incremental linear mobility vs. gate voltage for monolayer and bilayer InO_x transistors with low and high-temperature postannealing. **e** Optical bandgap of monolayer and bilayer 2D InO_x films extracted from UV-absorption with error bars of one standard deviation (SD). **f** Band diagram illustrating. quantum-confined band structure for monolayer and bilayer InO_x.

The current saturation and low hysteresis in these InO_x devices differentiate them from reports of highly conductive channels formed in recent reports of liquid metal 2D oxide TFTs[25]. The low hysteresis and steep subthreshold slope additionally suggest the potential for our liquid metal printed 2D InO_x to serve as a building block for high-performance thin-film circuits in a variety of large area electronics.

The exceptionally high electron mobility in these liquid metal printed transistors exceeds even that of In_2O_3 transistors fabricated by ALD[28–31] or DC sputtering[32], illustrating an advantage of the unique 2D grain morphology shown by HRTEM (Fig. 2c). A highly overlapped grain morphology has previously been observed to enhance percolative transport in highly conductive 2D nanosheet networks, such as CVD-grown graphene films[33]. The overlapping grain morphology is a unique 2D material feature of the InO_x channels presented here, since vacuum-deposited In_2O_3 otherwise tends towards microstructures with through-thickness grains with transport limited by grain boundary scattering[34]. Highly vertically overlapping grain morphologies can resolve this limitation, providing more efficient, inter-grain transport.

Importantly, unlike other printable 2D semiconductors such as MoS_2, WS_2, and WSe_2 that consist of ~ 1 – 10 μm scale nanosheets, 2D oxides offer the benefit of allowing large-scale continuous films (1 mm^2 – 1 cm^2) suitable for flexible device integration. This is essential because nanosheet networks of traditional TMD 2D materials can be limited by sheet-to-sheet charge transport, resulting in measured electronic mobility 10 – 100X lower than the single crystal mobility[35] as the area is scaled above the area of individual nanosheets. Figure 2d illustrates this trend of mobility vs. device area for reports of transistors with 2D semiconductor channels[36–51]. This shows the favorable large area scaling of 2D oxides that maintain high mobility while allowing for *printing-based-integration*. We expect that liquid metal printing can become an attractive low capital expenditure manufacturing technology for commercialization of these oxide devices, particularly if selective deposition processes can be applied to eliminate the need for subtractive etching processes[52].

Liquid metal printed 2D InO_x transistors deposited in a single printing step over large area substrates (>30 cm^2) achieve high mobility for both monolayer and bilayer channels. Figure 3a illustrates a comparison between postannealed (250 °C) bilayer and monolayer devices from multiple batches, which exhibit average low-field linear mobility of 17 cm^2 $V^{-1}s^{-1}$ and 2.3 cm^2 $V^{-1}s^{-1}$, respectively. Supplementary Table 2 reports the performance statistics for a single sample ($N = 13$), showing μ_{lin} of 19.6 ± 13.1 cm^2 $V^{-1}s^{-1}$, a μ_{sat} of 14.4 ± 11.7 cm^2 $V^{-1}s^{-1}$, and a V_{th} of −12.8 ± 4.8 V. Multiple subsequent device batches demonstrated similar performance, with average linear mobility of 15 – 19 cm^2 $V^{-1}s^{-1}$ and champion devices above 35 cm^2 $V^{-1}s^{-1}$ (Supplementary Fig. 8). Low-temperature processed bilayer devices exhibit peak mobility up to 37 cm^2 $V^{-1}s^{-1}$ (Table 1) as well as high on-currents (Supplementary Fig. 9) and excellent current saturation (Supplementary Fig. 10), even with ≤ 175 °C annealing. These processing conditions are comfortably within the limits of flexible substrates such as polyethylene. Compared with the highest performing bilayers, monolayers exhibit lower peak mobility (μ_0 ~ 3.0 cm^2 $V^{-1}s^{-1}$) but have more positive turn-on voltages. The enhanced transport in bilayer films can also be

Table 1. Transistor performance summary.

Channel	Thickness (nm)	Anneal Temperature (°C)	Linear Mobility, μ_0 ($cm^2V^{-1}s^{-1}$)	I_{on} / I_{off}	Turn on Voltage, V_{on} (V)	Saturation Mobility, μ_{sat} ($cm^2V^{-1}s^{-1}$)
Monolayer InO_x	2.2	175	3.0	10^5	−13	1.6
Monolayer InO_x	2.2	250	2.6	10^5	−9	2.0
Bilayer InO_x	4.9	175	37.3	10^6	−24	21.3
Bilayer InO_x	4.9	250	67.1	5×10^6	−12	44.6

Summary of device statistics shown for monolayer and bilayer liquid metal printed InO_x transistors.

justified as a result of the nanocrystalline grain structure observed by TEM, which produces significant overlap area between the vertically overlaid nanosheets.

Controlling electronic transport in 2D InO_x

Postannealing processes after the initial 2D oxide film transfer control electronic transport for the InO_x films of varying thickness. Bilayer and multilayer 2D InO_x transistors exhibit high on-current after deposition, but postannealing processes can be used read the free-carrier concentration and allow effective gating. Figure 3b, c illustrate transfer curves for bilayer and monolayer InO_x transistors with various postannealing temperatures, reaching optimal characteristics with high I_{on}/I_{off} near 200 °C postannealing. Sufficient thermal postannealing was observed to shift the turn-on voltage (V_{on}) from a depletion mode operation to enhancement mode operation and yield a steeper subthreshold slope. Thermal postannealing also enhances the low-field electronic mobility of the InO_x transistors (Fig. 3d), which is consistent with the higher crystalline fraction of annealed samples compared with the as-deposited thin films. Similar to the crystallinity, the mobility begins to reach its peak at 200–225 °C. We note that for predominant circuit applications, enhancement mode operation with V_{on} near 0 V is desirable. Recent work has shown that the free-carrier concentration of InO_x channels can also be controlled through back-channel passivation layers[53] and doping[54] to form ternary channel materials with improved bias-stress stability and uniformity. These dopants and passivation materials have been printed with liquid metals[20], offering an opportunity for multi-layered architectures that can leverage interfacial polarization effects known to induce 2D electron gases (2DEGs) in In_2O_3[55]. We expect that these material design strategies, in combination with improvements to the liquid metal printing process, can reduce device-to-device variability and enable greater commercial applicability of this technology.

Measurements of the optical properties of these InO_x films demonstrates the relationship between their 2D nature and resultant quantum confinement for modulating their electronic structure, as well as their ultra-transparency. InO_x naturally has lower optical absorption than would be predicted from its fundamental bandgap of approximately 2.92 eV due to the presence of dipole-forbidden optical transitions, which can effectively raise the bandgap by more than 0.8 eV by forcing direct transitions from well below the valence band maximum (VBM)[56]. Optical transmittance measurements revealed an average transmittance of 99.2% and 98.9% for monolayer and bilayer InO_x for the visible wavelength range of 400–800 nm. Tauc analysis of our 2D InO_x films suggests a significant widening in the optical bandgap (ΔE_g) for the thinnest 2D InO_x films, with an offset of approximately 90 - 150 meV between monolayer (2.2 nm) and bilayer (4.9 nm) InO_x (Supplementary Fig. 11). The Bohr radius of In_2O_3 is estimated to be approximately 2.35 nm (assuming $\varepsilon = 8.9$, $m_e^* = 0.3\ m_0$, and $m_h^* = 0.6\ m$)[57], suggesting that the blue-shifted absorption of monolayer films can be attributed to significant quantum confinement effects. Figure 3e illustrates the trend of E_g vs. postannealing, as extracted from direct bandgap[57] fits of the Tauc plots of absorption, showing a significant redshift after postannealing for both monolayers and bilayers. This is consistent with a lower free-carrier concentration and a diminishing Burstein-Moss effect. Indeed, the Burstein-Moss shift may also explain why these 2D InO_x films exhibit a smaller ΔE_g than would be expected based on the theory for 1-dimensional infinite quantum wells (QW)[58], which would predict $\Delta E_g \sim 250 - 300$ meV based on our thickness measurements:

$$\Delta E_G = \frac{h^2}{8L^2}\left(\frac{1}{m_e^*} + \frac{1}{m_h^*}\right) \quad (1)$$

Electrical characterization shows bilayer films exhibit a higher free-carrier concentration (n_0) than monolayer films, which should effectively increase their measured optical bandgap, mitigating the ΔE_g otherwise induced by quantum confinement. These observations also match the characteristics of InO_x transistors, suggesting a lower activation energy (E_a) for transport in bilayer films that exhibit less quantum confinement induced bandgap widening compared with monolayer films (Fig. 3f). For both cases of monolayer and bilayer InO_x, however, the activation energy can be effectively modulated to tune the turn-on voltage for various applications requiring enhancement mode operation for circuit-level integration.

Variable temperature Hall measurements were performed to characterize the electronic transport in *large area* 2D InO_x films of approximately 7 × 7 mm (Fig. 4a). Measurements of temperature-dependent resistivity illustrate the low activation energy of the highly conductive bilayer InO_x films, consistent with a trap-neutral level in proximity to the conduction band energy and the observed carrier concentration of approximately $1 \cdot 10^{19}\,cm^{-3}$. Hall measurements of these films show room-temperature mobility of approximately $12.9\,cm^2\ V^{-1}s^{-1}$. To fully understand the impact of postannealing and quantum confinement on transport in the liquid metal printed 2D InO_x, the electronic density of states (eDOS) was extracted using temperature-dependent transfer measurements of monolayer and bilayer thin-film transistors from 20 to 100 °C. The temperature-dependent measurements allowed for an extraction of the eDOS (Fig. 4b) through the method described elsewhere, based on the thermally activated low-field drain conductance[59]. Monolayer and bilayer films show distinct differences, with bilayer films exhibiting higher band tail slope but lower band edge concentration ($4 \cdot 10^{19}\,cm^{-3}$ for bilayers vs. $1.4 \cdot 10^{20}\,cm^{-3}$ for monolayers). These characteristics and the lower deep state concentration for bilayers are consistent with their higher mobility and improved subthreshold slope. A comparison of the printed 2D InO_x eDOS also shows a higher band edge concentration $5 \cdot 10^{20}\,cm^{-3}$ after 250 °C annealing, compared with $4 \cdot 10^{19}\,cm^{-3}$ for the sample annealed at 175 °C. Similarly, the InO_x channels annealed at 250 °C exhibit a steeper band tail slope consistent with their transition to a phase with higher crystalline fraction.

This method also allows comparison of the activation energy as a function of gate voltage for monolayer and bilayer films. This thermal activation energy E_A computed from the

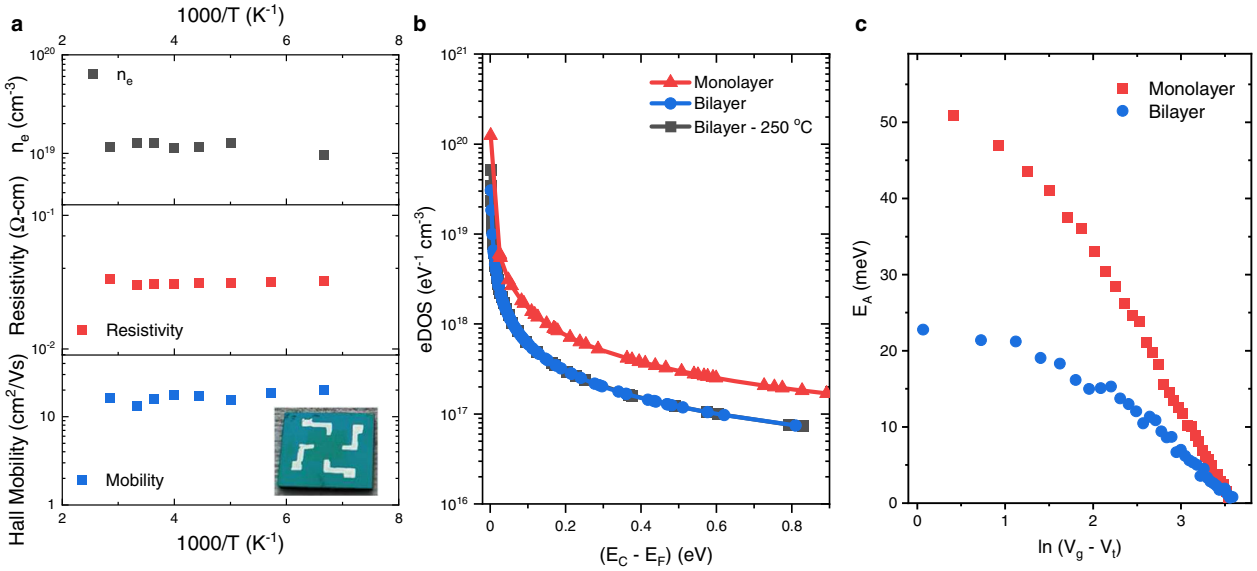

Fig. 4 Variable temperature Hall transport measurements and electronic density of states for 2D InO_x. a Temperature-dependent carrier concentration, resistivity, and Hall Mobility of liquid metal printed bilayer InO_x films. **b** Measured electronic density of states (eDOS) as a function of activation energy ($E_A = E_C - E_F$) for 2D printed InO_x. **c** Activation energy as a function of gate voltage for bilayer and monolayer InO_x transistors.

temperature-dependent measurements effectively describes the energy difference between the Fermi level and the delocalized states in the conduction band ($E_A = E_C - E_F$), as depicted in Fig. 3f. Figure 4c shows the lower activation energy for transport in bilayer films compared to monolayer films, which is consistent with the higher free-carrier concentration and the overlapping grain morphology discussed above. This behavior also corresponds well with the expected impact of quantum confinement, which would tend to raise the conduction band edge, as shown in Fig. 3f and force otherwise degenerate conductors into a semiconducting state.

CONCLUSION

The liquid metal printed 2D oxide transistors reported here demonstrate ultrahigh performance leveraging control of the electronic structure of nanoscale InO_x films as seen through the extracted eDOS. The 2D InO_x channels exhibit unprecedented performance for low-temperature, vacuum-free processed materials suitable for flexible electronics applications as well as high-performance circuits in active interposers. Combined with the transparency and known mechanical flexibility of these ultrathin films, the ultrahigh mobility electronic performance can drive potential commercial applications to wearable sensors, neuromorphic computing, and lightweight display technology. Future integration of this process into high-speed continuous printing technologies could unlock a new generation of high-performance flexible electronics.

METHODS

Dual-sided liquid metal printing process for InO_x

A silicon die with 100 nm of thermally grown SiO_2 was attached via thermal tape to each platen of a pneumatic thermal press preheated to 165 °C. A 0.5 g quantity of 99.995% purity indium metal (*Luciteria*) was placed in the center of the upward-facing die. The distance between the platens was decreased until the indium droplet contacted both dies. The pressure on the dies was then ramped up to 400 psi in 2 s. After 5 s, the pressure was released at the same rate. The dies were removed from the hot press within one minute. To remove any metal from the sample surface, each die was placed on a hot plate at 165 °C and a heat resistant silicone squeegee was scraped over the surface. The samples were then cleaned with an ethanol-wetted lint-free cloth. Monolayer films were deposited using SiO_2 wafers as both the donor and target substrates. Both the donor and target substrates had resulting monolayer films adhered after the liquid metal printing process. Bilayer films were deposited in a single step using low adhesion, plastic surfaces as the donor substrates to transfer both the front and back oxide films to the target SiO_2 substrate.

2D InO_x transistor fabrication

2D InO_x transistors were fabricated in a top contact, bottom gate architecture. A 10 min wet etch in 18% HCl was used to pattern the InO_x semiconductors (1000 × 500 µm). An adhesive Kapton shadow mask was used to define 1 × 1.5 mm source-drain electrodes with channel lengths from 50 – 500 µm. An *Anatech LTD Hummer 6.2* sputtering system was utilized to deposit 80 nm thick gold electrodes.

Electrical characterization

A semiconductor parameter analyzer (*Agilent E5260A*) was utilized for all transistor characterization. The electronic density of states (eDOS) was extracted from temperature-dependent measurements of low-field drain conductance from 23 °C to 120 °C. All other transfer and output characteristics shown here were captured at room temperature, in air. We observed that the yield of liquid metal printed InO_x semiconductor regions that were active and modulated by an applied gate voltage was approximately 88% across multiple batches. Incremental linear and saturation mobility were computed using the gradual channel approximation. Variable temperature Hall measurements (150 K–350 K) were performed with a 2D InO_x film deposited onto SiO_2 wafers and patterned into a Van der Pauw geometry with Au contacts. These samples were measured under vacuum (*MMR Technologies*) using a Joule Thomson stage and a 7200 gauss permanent magnet.

Materials characterization of 2D InO_x

X-ray diffraction (XRD) analysis was performed on 2D InO_x films deposited on Si wafers with 100 nm of thermally grown SiO_2 using a *Rigaku D/MAX 2000* diffractometer with Cu Kα radiation at scanning rates of either 1° or 0.1° per min. The InO_x nanosheets were characterized using a FEI *Tecnai F20* transmission electron microscope (TEM) at an accelerating voltage of 200 kV. The 2D InO_x films were directly printed onto TEM grids (carbon type-B 200-mesh Cu grids, *Ted Pella*). The printing process for the TEM samples entailed briefly and gently touching the liquid metal interface. Additionally, the cross-section of the nanosheets, prepared by the focused ion beam (FIB) lift-out technique using a scanning electron microscope

(SEM) dual-beam system (*Thermo Scientific Helios 5CX Dual Beam SEM/FIB*), was observed via TEM. A carbon layer with a thickness of ~20 nm was coated on the sample surface before Pt deposition in order to enhance the contrast and visibility of the InO_x films. XPS spectra were collected using a *Kratos Axis Supra XPS* at 10^{-9} Torr. A UV-Vis spectrophotometer (*DeNovix DS-11 FX+)* was used to observe the absorbance spectrum of the 2D InO_x films from 190 nm to 840 nm on glass and quartz substrates. InO_x bilayer film thicknesses were also measured with a high precision stylus profilometer (*Tencor D500*) with 0.4 Å vertical resolution and 5.0 Å repeatability, using the 40–60 nm combined step heights available after Au electrode deposition.

DATA AVAILABILITY

Data produced by this study are available from the corresponding author upon reasonable request.

Received: 13 September 2021; Accepted: 9 February 2022;
Published online: 14 March 2022

REFERENCES

1. Kim, H. S., Byrne, P. D., Facchetti, A. & Marks, T. J. High Performance Solution-Processed Indium Oxide Thin-Film Transistors. *J. Am. Chem. Soc.* **130**, 12580–12581 (2008).
2. Jang, J. et al. Transparent High-Performance Thin Film Transistors from Solution-Processed SnO2/ZrO2 Gel-like Precursors. *Adv. Mater.* **25**, 1042–1047 (2013).
3. Nomura, K. et al. Room-temperature fabrication of transparent flexible thin-film transistors using amorphous oxide semiconductors. *Nature* **432**, 488–492 (2004).
4. Wager, J. F. Transparent Electronics. *Science* **300**, 1245–1246 (2003).
5. Anthopoulos, T. D. Ultrathin channels make transistors go faster. *Nat. Mater.* **18**, 1033–1034 (2019).
6. Tiwari, N. et al. Indium Tungsten Oxide Thin Films for Flexible High-Performance Transistors and Neuromorphic Electronics. *ACS Appl. Mater. Interfaces* **10**, 30506–30513 (2018).
7. Li, S. et al. Nanometre-thin indium tin oxide for advanced high-performance electronics. *Nat. Mater.* **18**, 1091–1097 (2019).
8. King, P. D. C. et al. Surface Electron Accumulation and the Charge Neutrality Level in In_2O_3. *Phys. Rev. Lett.* **101**, 116808 (2008).
9. Si, M. et al. Why In2O3 Can Make 0.7 nm Atomic Layer Thin Transistors. *Nano Lett.* **21**, 500–506 (2021).
10. Gao, L. et al. Applications of Few-Layer Nb2C MXene: Narrow-Band Photodetectors and Femtosecond Mode-Locked Fiber Lasers. *ACS Nano* **15**, 954–965 (2021).
11. Zhang, Y. et al. Graphdiyne-Based Flexible Photodetectors with High Responsivity and Detectivity. *Adv. Mater.* **32**, 2001082 (2020).
12. Pei, J., Yang, J., Yildirim, T., Zhang, H. & Lu, Y. Many-Body Complexes in 2D Semiconductors. *Adv. Mater.* **31**, 1706945 (2019).
13. Son, Y., Frost, B., Zhao, Y. & Peterson, R. L. Monolithic integration of high-voltage thin-film electronics on low-voltage integrated circuits using a solution process. *Nat. Electron.* **2**, 540–548 (2019).
14. Datta, R. S. et al. Flexible two-dimensional indium tin oxide fabricated using a liquid metal printing technique. *Nat. Electron.* **3**, 51–58 (2020).
15. Poodt, P. et al. Spatial atomic layer deposition: A route towards further industrialization of atomic layer deposition. *J. Vac. Sci. Technol. A* **30**, 010802 (2012).
16. Fukuda, K. & Someya, T. Recent Progress in the Development of Printed Thin-Film Transistors and Circuits with High-Resolution Printing Technology. *Adv. Mater.* **29**, 1602736 (2017).
17. Scheideler, W. J., Kumar, R., Zeumault, A. R. & Subramanian, V. Low-Temperature-Processed Printed Metal Oxide Transistors Based on Pure Aqueous Inks. *Adv. Funct. Mater.* **27**, 1606062 (2017).
18. Baby, T. T. et al. A General Route toward Complete Room Temperature Processing of Printed and High Performance Oxide Electronics. *ACS Nano* **9**, 3075–3083 (2015).
19. MacDonald, W. A. et al. Latest advances in substrates for flexible electronics. *J. Soc. Inf. Disp.* **15**, 1075–1083 (2007).
20. Zavabeti, A. et al. A liquid metal reaction environment for the room-temperature synthesis of atomically thin metal oxides. *Science* **358**, 332–335 (2017).
21. Zhao, S., Zhang, J. & Fu, L. Liquid Metals: A Novel Possibility of Fabricating 2D Metal Oxides. *Adv. Mater.* **33**, 2005544 (2021).
22. Alsaif, M. M. Y. A. et al. 2D SnO/In2O3 van der Waals Heterostructure Photodetector Based on Printed Oxide Skin of Liquid Metals. *Adv. Mater. Interfaces* **6**, 1900007 (2019).
23. Li, Q. et al. Gas-mediated liquid metal printing toward large-scale 2D semiconductors and ultraviolet photodetector. *Npj 2D Mater. Appl* **5**, 1–10 (2021).
24. Jannat, A. et al. Printable Single-Unit-Cell-Thick Transparent Zinc-Doped Indium Oxides with Efficient Electron Transport Properties. *ACS Nano* **15**, 4045–4053 (2021).
25. Daeneke, T. et al. Wafer-Scale Synthesis of Semiconducting SnO Monolayers from Interfacial Oxide Layers of Metallic Liquid Tin. *ACS Nano* **11**, 10974–10983 (2017).
26. Buchholz, D. B. et al. The Structure and Properties of Amorphous Indium Oxide. *Chem. Mater.* **26**, 5401–5411 (2014).
27. Socratous, J. et al. Electronic Structure of Low-Temperature Solution-Processed Amorphous Metal Oxide Semiconductors for Thin-Film Transistor Applications. *Adv. Funct. Mater.* **25**, 1873–1885 (2015).
28. Kim, H. Y. et al. Low-Temperature Growth of Indium Oxide Thin Film by Plasma-Enhanced Atomic Layer Deposition Using Liquid Dimethyl(N-ethoxy-2,2-dimethylpropanamido)indium for High-Mobility Thin Film Transistor Application. *ACS Appl. Mater. Interfaces* **8**, 26924–26931 (2016).
29. Lee, J.-H. et al. Metastable Rhombohedral Phase Transition of Semiconducting Indium Oxide Controlled by Thermal Atomic Layer Deposition. *Chem. Mater.* **32**, 7397–7403 (2020).
30. Ma, Q. et al. Atomic-Layer-Deposition of Indium Oxide Nano-films for Thin-Film Transistors. *Nanoscale Res. Lett.* **13**, 1–8 (2018).
31. Lee, J. et al. High mobility ultra-thin crystalline indium oxide thin film transistor using atomic layer deposition. *Appl. Phys. Lett.* **113**, 112102 (2018).
32. Lee, M.-H. et al. 15.4: Excellent Performance of Indium-Oxide-Based Thin-Film Transistors by DC Sputtering. *SID Symp. Dig. Tech. Pap.* **40**, 191–193 (2009).
33. Min, S. Y. et al. Two-dimensional sheet resistance model for polycrystalline graphene with overlapped grain boundaries. *FlatChem* **7**, 19–25 (2018).
34. Frischbier, M. V. et al. Influence of dopant species and concentration on grain boundary scattering in degenerately doped In2O3 thin films. *Thin Solid Films* **614**, 62–68 (2016).
35. Kelly, A. G. et al. All-printed thin-film transistors from networks of liquid-exfoliated nanosheets. *Science* **356**, 69–73 (2017).
36. Lu, S. et al. Flexible, Print-in-Place 1D–2D Thin-Film Transistors Using Aerosol Jet Printing. *ACS Nano* **13**, 11263–11272 (2019).
37. Kim, S. et al. High-mobility and low-power thin-film transistors based on multilayer MoS2 crystals. *Nat. Commun.* **3**, 1011 (2012).
38. Kim, T.-Y. et al. Electrical Properties of Synthesized Large-Area MoS_2 Field-Effect Transistors Fabricated with Inkjet-Printed Contacts. *ACS Nano* **10**, 2819–2826 (2016).
39. Woo, Y. et al. Large-Area CVD-Grown MoS_2 Driver Circuit Array for Flexible Organic Light-Emitting Diode Display. *Adv. Electron. Mater.* **4**, 1800251 (2018).
40. Nouri, M., Asad, M. & Wong, W. S. Fabrication of Thin-Film Transistors Using Large-Area Exfoliation of Single-Crystal MoS_2 Layers and Inkjet-Printing. in *2019 IEEE International Flexible Electronics Technology Conference (IFETC)* 1–3 (2019).
41. Kim, T.-Y. et al. Transparent Large-Area MoS_2 Phototransistors with Inkjet-Printed Components on Flexible Platforms. *ACS Nano* **11**, 10273–10280 (2017).
42. Hong, S. et al. Highly sensitive active pixel image sensor array driven by large-area bilayer MoS_2 transistor circuitry. *Nat. Commun.* **12**, 3559 (2021).
43. Nam, H. et al. MoS_2 Transistors Fabricated *via* Plasma-Assisted Nanoprinting of Few-Layer MoS_2 Flakes into Large-Area Arrays. *ACS Nano* **7**, 5870–5881 (2013).
44. Choi, M. et al. Flexible active-matrix organic light-emitting diode display enabled by MoS_2 thin-film transistor. *Sci. Adv.* **4**, eaas8721 (2018).
45. Zhang, T. et al. High performance few-layer MoS_2 transistor arrays with wafer level homogeneity integrated by atomic layer deposition. *2D Mater.* **5**, 015028 (2017).
46. Zhang, S. et al. Wafer-scale transferred multilayer MoS_2 for high performance field effect transistors. *Nanotechnology* **30**, 174002 (2019).
47. Movva, H. C. P. et al. High-Mobility Holes in Dual-Gated WSe_2 Field-Effect Transistors. *ACS Nano* **9**, 10402–10410 (2015).
48. Xian, G. et al. Scalable preparation of water-soluble ink of few-layered WSe_2 nanosheets for large-area electronics. *Chin. Phys. B* **29**, 066802 (2020).
49. Esfandiari, M., Kamaei, S., Rajabali, M. & Mohajerzadeh, S. High-performance large-area WS_2 -based transistors by a novel tin-oxide assisted liquid-phase exfoliation: doping adjustment by plasma treatment. *2D Mater.* **8**, 025013 (2021).
50. Yue, Y. et al. Two-Dimensional High-Quality Monolayered Triangular WS_2 Flakes for Field-Effect Transistors. *ACS Appl. Mater. Interfaces* **10**, 22435–22444 (2018).
51. Yang, L. et al. Chloride Molecular Doping Technique on 2D Materials: WS_2 and MoS_2. *Nano Lett.* **14**, 6275–6280 (2014).
52. Carey, B. J. et al. Wafer-scale two-dimensional semiconductors from printed oxide skin of liquid metals. *Nat. Commun.* **8**, 14482 (2017).
53. Ding, Y. et al. High-Performance Indium Oxide Thin-Film Transistors With Aluminum Oxide Passivation. *IEEE Electron Device Lett.* **40**, 1949–1952 (2019).

54. Lee, S.-H., Kim, T., Lee, J., Avis, C. & Jang, J. Solution-processed gadolinium doped indium-oxide thin-film transistors with oxide passivation. *Appl. Phys. Lett.* **110**, 122102 (2017).
55. Kuang, Y. et al. Band Alignment and Enhanced Interfacial Conductivity Manipulated by Polarization in a Surfactant-Mediated Grown κ-Ga2O3/In2O3 Heterostructure. *ACS Appl. Electron. Mater.* **3**, 795–803 (2021).
56. Walsh, A. et al. Nature of the Band Gap of In_2O_3 Revealed by First-Principles Calculations and X-Ray Spectroscopy. *Phys. Rev. Lett.* **100**, 167402 (2008).
57. Hamberg, I. & Granqvist, C. G. Evaporated Sn-doped In_2O_3 films: Basic optical properties and applications to energy-efficient windows. *J. Appl. Phys.* **60**, R123–R160 (1986).
58. Dingle, R. Confined carrier quantum states in ultrathin semiconductor heterostructures. in *Festkörperprobleme 15: Plenary Lectures of the Divisions "Semiconductor Physics", "Low Temperature Physics", "Metal Physics" of the German Physical Society Münster, March 17–21, 1975* (ed. Queisser, H. J.) 21–48 (Springer, 1975).
59. Bubel, S. & Chabinyc, M. L. Model for determination of mid-gap states in amorphous metal oxides from thin film transistors. *J. Appl. Phys.* **113**, 234507 (2013).

ACKNOWLEDGEMENTS

Andrew Hamlin was supported by an NSF Graduate Research Fellowship. The manuscript was written through contributions of all authors. All authors have given approval to the final version of the manuscript.

AUTHOR CONTRIBUTIONS

W.J.S. and A.B.H. conceived the concept of the project. W.J.S. supervised the project and wrote the manuscript. A.B.H. fabricated and characterized the devices. J.E.H. analyzed the XPS data. Y.Y. completed and analyzed XRD and TEM studies. M.S.R. assisted in writing and editing of the manuscript. All authors have given approval to the final version of the manuscript.

COMPETING INTERESTS

The authors declare no competing interests.

ADDITIONAL INFORMATION

Supplementary information The online version contains supplementary material available at https://doi.org/10.1038/s41699-022-00294-9.

Correspondence and requests for materials should be addressed to William J. Scheideler.

Reprints and permission information is available at http://www.nature.com/reprints

Publisher's note Springer Nature remains neutral with regard to jurisdictional claims in published maps and institutional affiliations.